Effects of Chemical Composition on Nanocrystallization Kinetics, Microstructure and Magnetic Properties of Finemet-Type Amorphous Alloys

UNIVERSITÀ DEGLI STUDI DI TORINO

Effects of Chemical Composition on Nanocrystallization Kinetics, Microstructure and Magnetic Properties of Finemet-Type Amorphous Alloys

Hossein Asghari Shivaee[1,2], Alberto Castellero[1,*], Paola Rizzi[1], Paola Tiberto[3], Hamid Reza Madaah Hosseini[4], Marcello Baricco[1]

[1]Dipartimento di Chimica and NIS, Università di Torino, Torino, Italy

[2]Institute for Nanoscience and Nanotechnology, Sharif University of Technology, Tehran, Iran

[3]INRIM, Electromagnetism Division, Torino, Italy

[4]Department of Materials Science and Engineering, Sharif University of Technology, Tehran, Iran

[*] Corresponding author. Tel. +39 0116707097; fax: +39 0116707855. E-mail: alberto.castellero@unito.it

Abstract

In this study, the kinetics of nanocrystallization of amorphous $Fe_{73.5}Si_{13.5}B_9Nb_3Cu_1$ (F1) and $Fe_{77}Si_{11}B_9Nb_{2.4}Cu_{0.6}$ (F2) alloys is investigated. The microstructure and magnetic properties of the nanocrystalline alloys are compared.

The crystallization temperature of F2 alloy is shifted towards lower temperatures with respect to F1. Thus, the crystalline volume fraction and the crystalline grain size at specific annealing temperature for the F2 alloy are higher than for the F1 alloy, accounting for the higher coercive force of F2 alloy with respect to the one of F1 alloy. According to isoconversional methods, the activation energy for crystallization is variable as a function of transformed fraction because of the continuous changes in chemical composition during the transformation. Mean values of 350 and 290 kJ/mol are obtained for F1 and F2, respectively. Microstructural observations confirm that minor changes in chemical composition affect the kinetics and final microstructure of the nanocrystalline alloy, that determine the observed magnetic properties.

Keywords: amorphous materials, crystallization, grain growth, magnetic properties, thermal analysis.

1. INTRODUCTION

Nanocrystalline alloys obtained by devitrification of Fe-based amorphous precursors have been extensively studied due to their excellent soft magnetic properties [1-5]. Among these nanocrystalline materials, Finemet (Fe–Si–B–Nb–Cu) alloy [6] exhibit ultrasoft magnetic properties, which are ideal for applications such as transformer cores, choke coils and EMI filters [1-2]. After suitable heat treatment, ultrafine magnetic bcc Fe(Si) nanograins form within the amorphous matrix. Increasing the heat treatment temperature, boride phases are formed with consequent deterioration of the soft magnetic properties. The formation of Cu-rich clusters as nucleation sites before crystallization [5], and the grain growth inhibiting effect of Nb atoms [7,

8], leads to a nanoscale microstructure. According to random anisotropy model [9,10], this microstructure is the main reason for magnetic softness of the alloy.

Changes in the type or content of the elements in the amorphous alloy are known to be the way for improving magnetic, corrosion, and mechanical properties [11-16]. Substitution or change in the alloy content could also affect the crystallization kinetics and microstructure of partially crystallized samples. For example, Cu content affects the size and distribution of grains in partially crystallized Finemet alloys [17] and substitution of Fe with Co reduces the crystallization onset temperature up to 40 K [18].

The research interest in the Finemet-type alloys has been recently revitalized by several papers focusing on preparation routes leading to the optimal microstructure directly in the as quenched melt [19], studying the effects of microalloying [20-22], internal stress [23] and structural relaxation [24] on the magnetic properties.

Due to the dependence of the magnetic properties of Finemet-type alloys on the crystallization kinetics [25-26], in the present work we apply an advanced isoconversional method [27] for determining the complete kinetic parameters (kinetic triplet) related to the nanocrystallization of Finemet-type alloys. We compare the results obtained for the original Finemet alloy $Fe_{73.5}Si_{13.5}B_9Nb_3Cu_1$ (F1) with those of $Fe_{77}Si_{11}B_9Nb_{2.4}Cu_{0.6}$ (F2) in which an improved magnetic flux density can be achieved by small composition variation without any replacement in the alloying elements [28].

2. EXPERIMENTAL PROCEDURES

Ingot of master alloys were prepared by arc melting under protective argon atmosphere and the actual composition was checked by inductivity coupled plasma (ICP) and EDAX analysis. Amorphous ribbons, prepared by single roller melt spinning method under protective argon atmosphere with copper wheel speed of 30 m/s, have cross section of 0.02 mm×1.00 mm.

Isothermal heat treatments of the samples were carried out at 350, 450, 550, 650 and 750 °C. To prevent oxidation during the heat treatment, the samples were sealed in quartz ampoules after repeated evacuation sequences. The ampoules containing the sample were placed within the uniform heating zone of the furnace and annealed for 1 hr. The heating rate of the furnace was 5 °C/min.

Structural changes of the isothermally annealed ribbons were analyzed using Philips PW 1830 X-ray diffractometer with Cu Kα radiation (λ=1.54056 Å). The scattering domain size of the crystalline phases was estimated by analyzing the peak broadening with the Williamson-Hall model [29]. The experimental diffraction peaks around 45° were fitted with two different pseudo-Voigt functions in order to separate the contributions of the amorphous and crystalline phase. The crystalline fraction was obtained from the ratio of the integral intensity of the crystalline contribution to the total integral intensity:

$$V_{cryst} = \frac{I_{cryst}}{I_{cryst} + I_{am}} \qquad (1)$$

where I_{cryst} and I_{am} are the integral intensities of the crystalline and amorphous phases, respectively [30].

The microstructures obtained after annealing were characterized by means of a transmission electron microscope (TEM) JEOL JEM 3010. Samples were prepared by electropolishing in a Struers Tenupol double-jet operating at 10V, with an electrolyte of HNO_3 and ethanol, at -20 °C.

The nanocrystallization kinetics was investigated with a Mettler Toledo DSC-1 at the heating rates of 5, 10, 20, 40 and 80 °C/min. The temperature was calibrated with an error below 1 °C, using indium standard samples for all the heating rates. Magnetic properties of the samples were measured using conventional fluxmetric method.

3. KINETIC ANALYSIS

The kinetics of nanocrystallization was studied under non-isothermal conditions because of several advantages, such as rapidity and extended temperature range of measurements, compared to isothermal ones [31]. The transformation rate of a solid-state reaction in non-isothermal conditions can be described according to [32]:

$$d\alpha/dT = (A/\beta)\exp(-E/RT)f(\alpha), \quad (2)$$

where α is the transformed fraction, A is the pre-exponential factor, β is the heating rate, E is the activation energy, R is the universal gas constant and f(α) is a function of α according to a reaction model. For a specific degree of the conversion fraction (α), a corresponding $T_{\alpha,i}$ can be identified for each heating rate β_i.

Integration of equation 2 up to a defined value of α, corresponding to temperature T_α results in:

$$g(\alpha) \equiv \int_0^\alpha \frac{d\alpha}{f(\alpha)} = \frac{A}{\beta}\int_0^{T_\alpha} \exp(-E/RT)dT = \frac{A}{\beta} I(E,T), \quad (3)$$

where *g(α)* is the integral form of 1/*f(α)* and *I(E,T)* is an energy-temperature integral that does not have an analytical solution. To solve it, several approximations were suggested [32]. Accordingly, several models such as Kissinger-Akahira-Sunose (KSA) [33], Flyn-Wall-Ozawa (FWO) [34], Tang [35], Coats [36] and Starink [37,38] can be used to calculate the activation energy. As an example, Doyle's approximations leads to the Ozawa's isoconversional method in the form:

$$\ln(\beta_i) = C - \frac{1.05E_\alpha}{RT_{\alpha,i}} \quad (4)$$

where C a constant. From the plot of $\ln(\beta_i)$ against $1/T_{\alpha,i}$, the activation energy, E_α, can be determined from a linear regression slope.

Vyazovkin [27] developed an advanced isoconversional method that uses an accurate numerical integration. Assuming that the reaction model does not dependent on the heating rate [34,35], eq, 3 can be written for each value of α and different heating rates β_i (i = 1,…, n):

$$(A_\alpha/\beta_1)I(E_\alpha, T_{\alpha,1}) = (A_\alpha/\beta_2)I(E_\alpha, T_{\alpha,2}) = \ldots = (A_\alpha/\beta_n)I(E_\alpha, T_{\alpha,n}) \quad (5)$$

After rearranging, eq. 5 can be rewritten as

$$\sum_i^n \sum_{j\neq i}^n \left[I(E_\alpha, T_{\alpha,i})\beta_j\right] / \left[I(E_\alpha, T_{\alpha,j})\beta_i\right] = n(n-1) \quad (6)$$

Since the T_α values are measured with some experimental error, eq. 6 can be only approximately satisfied. Consequently, values of the activation energy can be estimated by minimising the following expression [39]

$$n(n-1) - \sum_i^n \sum_{j\neq i}^n \left[I(E_\alpha, T_{\alpha,i})\beta_j\right] / \left[I(E_\alpha, T_{\alpha,j})\beta_i\right] \quad (7)$$

4. RESULTS AND DISCUSSION

X-ray diffraction patterns (Fig. 1) and SAD patterns (not shown) of the as quenched samples confirm that the melt spun precursors are fully amorphous. Typical DSC curves obtained during the heating cycle of as quenched F1 and F2 samples at the heating rate of 20 °C/min are presented in Fig. 2. A small inflection in the DSC curve, corresponding to the Curie temperature, can be observed at 392 °C and 377 °C for F1 and F2, respectively. For both alloy, the DSC curves involve two exothermal peaks, where the first peak corresponds to the crystallization of bcc-Fe(Si) nano grains and the second one is related to the formation of boride phases. According to the literature [17], copper clustering, which provides a high number density of nucleation sites, is expected to occur just before the primary crystallization peaks. For the first transformation, the onset temperature, the peak temperature and the heat of were determined from the DSC curves and the obtained values are reported in Fig 2.

The structural changes induced by annealing of the two alloys at selected temperatures for 1 hour were detected by X-ray diffraction, and the results are shown in Fig. 1. Below 350 °C, diffraction patterns of both samples show the typical halo of an amorphous phase. An increase of the annealing temperature above 350 °C promotes the formation of a sharp diffraction peak at $2\theta \sim 45°$, corresponding to the (110) reflection of bcc-(Fe,Si) phase, whose height increases with the increase of the annealing temperature. A further increase of the annealing temperature above 550 °C leads to the formation of boride phases. The higher value of the scattering domain size (table 1) of the nanocrystalline bcc phase observed for the F2 alloy, with respect to that of the F1 alloy for the same annealing conditions, is related to the lower Nb content that reduces the crystallization onset temperature in F2 alloy. As expected, the mean scattering domain size of the Fe(Si) phase increases for both alloys with increasing the annealing temperatures. The crystalline

volume fraction, estimated with eq. 1, is higher for the annealed F2 alloy with respect to the annealed F1 alloy (Table 1), as a consequence of the lower primary crystallization temperature of F2 alloy. By increasing the heat treatment temperature for both samples, the crystalline volume fraction increases. In the framework of a simple geometrical model, using the average grain size and the amorphous volume fraction in the samples, the intergranular spacing was estimated and the results are shown in Table 1. For F2 alloy, the lower value of the intergranular spacing is a direct consequence of Nb content reduction, which allows the growth of the nanograins formed during primary crystallization.

According to XRD and DSC results, samples of F1 and F2 alloys annealed at 550 °C for 1 hour likely completed nanocrystallization processes.

TEM bright field images of the F1 and F2 samples annealed at 550 °C for 1 hour, together with the corresponding selected area electron diffraction pattern (SAD), are shown in Fig. 3(a) and Fig. 3(b), respectively. In addition, an HRTEM image clearly showing a bcc-(Fe,Si) nanograin embedded in the amorphous matrix is shown in the inset of Fig. 3(a). Both samples contain a high density of isotropic bcc-(Fe,Si) crystallites. The mean values of the crystallites size measured from TEM images are about 15-20 and 25-50 nm for F1 and F2 alloy, respectively, These values are in good agreement with those obtained for the mean scattering domain size from XRD measurement for the F1 sample (i.e. 22±2 nm), while are definitely larger for the F2 sample. This could be related to the presence, in the F2 sample, of crystal defects so that the coherent scattering domain measured by XRD is not related to the whole crystal but just to a subgrain bounded by dislocations [40]. The hysteresis loop and magnetic properties of F1 and F2 alloys annealed at 550 °C for 1 hour are shown in Fig. 4 and Table 2, respectively. Results show that the F2 sample exhibits a higher remanence due to the higher Fe content. The higher

coercivity of alloy F2 with respect to F1 can be explained, on the basis of the random anisotropy model [9], by the coarser microstructure. For the same reason, values of coercivity (table 2) observed for both alloys are slightly higher than those previously reported in the literature for similar nanocrystalline alloys [4,5,7].

On the basis of the experimental observations, it is clear that small changes in chemical composition may cause considerable changes on the microstructure and nanocrystallization kinetics of the amorphous alloys. In order to estimate kinetic parameters, DSC analyses of the amorphous samples were performed at various heating rates and the results are shown in Fig. 5 for both alloys. The results show that increasing the heating rate, the onset and peak temperatures are shifted towards higher values due to the thermal activated behavior of the nanocrystallization process. From DSC results, activation energy as a function of transformed fraction were calculated according to KSA, FWO, Tang, Starink and Vyazovkin isoconversional methods and the results are shown in Fig. 6.

The activation energies are not constant as a function of the transformed fraction. An increase of $E(\alpha)$ with α is seen for low α values, which corresponds to the initial stage of crystallization (mainly nucleation). It is worth to note that the presence of quenched-in nuclei in the amorphous precursor, due to limited cooling rate during glass formation, reduces the activation energy at the beginning of the phase transformation [41-42]. The different apparent activation energies assessed for the two alloys can be explained by the difference between the crystallization temperature (T_p) and the Cu clustering temperature (T_{clust}). Even if the T_{clust} was not experimentally determined in this work, it is known [17] that Cu clusters act as nucleation sites, so their density and distribution is expected to affect the kinetics of crystallization and the corresponding final microstructure. It is also known [17] that the nanocrystallization peak

temperature has little dependence on Cu content, while Cu clustering temperature significantly decreases as the Cu content increases. In the case of larger temperature difference (T_p - T_{clust}) between crystallization onset and Cu clustering, there is enough time for clusters to coarsen until the nucleation of primary Fe(Si) nanocrystals occurs [17].

For transformed fractions in the range of 0.1-0.5, the activation energy changes with different slope for two alloys. The mean value of activation energy was estimated to be 350 and 290 $kJmol^{-1}$ for F1 and F2 alloys, respectively (error 5%). The difference of activation energy of F1 and F2 alloys is mainly related to the amount of Nb and Cu elements in the alloy, that affects the nucleation and growth processes. In this stage of crystallization, as the Fe(Si) phase forms, Nb and B atoms are rejected from the Fe(Si) crystallites. The formation of a Nb rich shell around nano grains [8], due to a small diffusion coefficient, hinders further growth and thus increases the apparent activation energy. Immediately after nucleation, the nuclei are embedded into an amorphous matrix and interface controlled growth is dominant. When solute fluxes through the interface are driven by diffusion, the growth process becomes diffusion controlled. So, as the nanocrystallization proceeds, the growth mechanism changes from interface controlled to diffusion controlled [43]. The difference in the increase of activation energy as a function of α for F1 and F2 alloys in this stage, can be related to the relative contribution of diffusion and interface controlled growth. For transformed fractions in the range $0.5<\alpha<0.7$, the activation energy increases similarly for both alloys, suggesting a similar crystallization mechanism. The effect of "soft impingement" on the growth mechanism is an important factor at the final stages of crystallization ($\alpha>0.7$). It arises from the overlapping of concentration gradient ahead of the surface of neighbouring crystalline particles. The activation energy is almost constant at this stage.

These results confirm that the nanocrystallization in Finemet-type alloys is a complex and multistep reaction. Due to the nanocrystallization complexities and to the effect of the initial condition of amorphous precursors, a broad range of values for the activation energy have been reported [44-47] for alloys with similar composition, which are difficult to be compared with results obtained in the present study.

In order to investigate the kinetics in more details, the pre-exponential factor and the reaction model were determined. Pre-exponential factor, A , was evaluated using the compensating correlation of E and A or so-called artificial isokinetic relationship (IKR) that occurs on fitting various reaction model, $g_i(\alpha)$, to the same set of non-isothermal kinetic data [48]:

$$\log A_i = aE_i - b, \tag{8}$$

where, a and b are constants. A_i and E_i are Arrhenius parameters associated with a particular reaction model, $g_i(\alpha)$, assumed to describe the transformation process. The A_i and E_i values for each particular $g_i(\alpha)$ were calculated using Eq. 3. Accordingly, the values of a and b obtained from the slope of log A_i versus E_i are $6.73 \times 10^{-5} \pm 0.08 \times 10^{-5}$, 0.98 ± 0.24 for F1 alloy and $7.24 \times 10^{-5} \pm 0.02 \times 10^{-5}$, 0.33 ± 0.14 for F2 alloy, respectively. Thus the values of pre-exponential factor corresponding to mean values of activation energies for F1 (E = 350 kJmol^{-1}) and F2 (E = 290 kJmol^{-1}) are $3.8 \times 10^{22} \pm 1.1 \times 10^{22}$ min^{-1} and $7.9 \times 10^{20} \pm 1.6 \times 10^{20}$ min^{-1}. Knowing the pre-exponential factor, the integral form of the reaction model, $g(\alpha)$, corresponding to different heating rates could be reconstructed numerically using Eq. 3, for each value of E_α. Gorbachev approximation [49] was used to solve the temperature integral $I(E,T)$.

Numerically reconstructed form of $g(\alpha)$ at heating rate of 5 K/min are shown in Fig. 7 for both alloys. Solid lines were plotted according to different theoretical models [50], indicated by

numbers on the curves. At low transformed fractions, the experimental $g(\alpha)$ can be reproduced assuming a three dimensional phase boundary reaction and a power law reaction for F1 and F2, respectively. Successively, at high transformed fraction, the experimental $g(\alpha)$ of both alloys follow trends that are only qualitatively compatible with diffusion controlled mechanisms. On the basis of TEM images (Fig. 3), showing rounded and isotropic crystallites, a three dimensional grain growth can be assumed, in accordance with the literature [5, 43, 51]. The limited agreement between the experimental $g(\alpha)$ and the simple models is due to the approximations used here, since separation of the different mechanisms operating at various stages of the transformation was not taken in account. In fact, the experimental reaction models, $g(\alpha)$, for alloys F1 and F2 are plotted in Fig. 7 as a function of a transformed fraction, α, that is related to the whole transformation, *amorphous(1)*$\rightarrow$ α*-Fe + amorphous(2)*, irrespectively of the mechanism. Furthermore, each single reaction model represented by the lines is assumed to be representative of the whole transformation.

In conclusion, the current analysis confirms the complex nature of nanocrystallization in Finemet alloys [5, 8, 17, 43, 52] and the strong effect of small chemical composition changes on the transformation mechanism, suggesting great caution in the interpretation of results [48].

5. CONCLUSIONS

Effects of chemical composition on the nanocrystallization kinetics, microstructure and magnetic properties of $Fe_{73.5}Si_{13.5}B_9Nb_3Cu_1$ (F1) and $Fe_{77}Si_{11}B_9Nb_{2.4}Cu_{0.6}$ (F2) alloys were investigated. . The lower Nb content in F2 alloy shifts the crystallization onset temperature at lower values with respect to F1 alloy and promotes the grain growth, leading to a higher coercive force for this

alloy. Variable activation energies as a function of transformed fraction were calculated. Differences in the activation energy for both alloys are a consequence of chemical composition changes, that affect nucleation and growth processes. Numerical reconstruction of the reaction model using experimental data showed that nanocrystallization mechanism could not be described with a single theoretical model, confirming the complexity of nanocrystallization process.

ACKNOWLEDGMENTS

H.A.S. acknowledges Università di Torino for providing experimental facilities used for this work.

REFERENCES

[1] D. Prabhu, A. Narayanasamy and K. Chattopadhyay, *J. Non-Cryst. Solids* **353**, 1577 (2007).

[2] M. Sakurai, M. Matsuura, S. H. Kim, Y. Yoshizawa, K. Yamauchi and K. Suzuki, *Mater. Sci. Eng. A* **179-180**, 469 (1994).

[3] M. Baricco, C. Antonione, P. Allia, P. Tiberto and F. Vinai, *Mater. Sci. Eng. A* **179-180**, 572 (1994).

[4] P. Allia, M. Baricco, E. Bonetti, L. Del Bianco, P. Tiberto, G. Valdré and F. Vinai, *Nanostruct. Mat.* **3**, 433 (1993).

[5] K. Hono, K. Hiraga, Q. Wang, A. Inoue and T. Sakman, *Acta Metall.Mater.* **40**, 2137 (1992).

[6] Y. Yoshizawa and K. Yamauchi, *Mater. Trans. JIM* **31**, 307 (1990).

[7] G. Herzer, *J. Magn. Magn. Mater.* **157-158**, 133 (1996).

[8] W. Lefebvre, S. Morin-Grognet and F. Danoix, *J. Magn. Magn. Mater.* **301**, 343 (2006).

[9] G. Herzer, *IEEE Trans. Magn.* **25**, 3327 (1989).

[10] A. Hernando, M. Vazquez, T. Kulik and C. Prados, *Phys. Rev. B* **51**, 3581 (1995).

[11] C. Li, X. Tian, X. Chen, A. G. Ilinsky and L. Shi, *Mater. Lett.* **60**, 309 (2006).

[12] F. Mazaleyrat, Zs. Gercsi, J. Ferenc, T. Kulik and L. K. Varga, *Mater. Sci. Eng. A* **375–377**, 1110 (2004).

[13] N. D. Tho, N. Chau, S. C. Yu, H. B. Lee, N. D. The and L. A. Tuan, *J. Magn. Magn. Mater.* **304**, 195 (2006).

[14] N. Chau, N. Q. Hoa, N. D. Tho and P. Q. Niem, *J. Magn. Magn. Mater.* **304**, 179 (2006).

[15] C. F. Conde, M. Millan and A. Conde, *J. Non-Cryst. Solids* **232-234**, 346 (1998).

[16] N. Iturriza, L. Fernandez, M. Ipatov, A. R. Pierna, J. J. del Val, A. Chizhik and J. Gonzalez, *J. Magn. Magn. Mater.* **316**, 74 (2007).

[17] M. Ohnuma, K. Hono, S. Linderoth, J. S. Pedersen, Y. Yoshizawa and H. Onodera, *Acta Mater.* **48**, 4783 (2000).

[18] J. M. Borrego, C. F. Conde, A. Conde and J. M. Greneche, *J. Non-Cryst. Solids* **287**, 120 (2001).

[19] G. Pozo López, L.M. Fabietti, A.M. Condó and S.E. Urreta, *J. Magn. Magn. Mater*. **322**, 3088 (2010).

[20] Z.J. Yan, B.R. Bian, Y. Hu, S.E. Dang, L.T. Xia and Y.M. Wang, J. Magn. Magn. Mater. **322**, 3359 (2010).

[21] P.H. Zhou, J.L. Xie, D.F. Liang and L.J. Deng, J. Magn. Magn. Mater. **322**, 3290 (2010)

[22] J.M. Silveyra, E. Illeková, P. Švec, D. Janičkovič, A. Rosales-Rivera and V.J. Cremaschi, *Physica B* **405**, 2720 (2010).

[23] J. Moulin, F. Mazaleyrat, A. Mendeza and E. Dufour-Gergam, *J. Magn. Magn. Mater*. **322**, 1275 (2010).

[24] S. Kaloshkin, M. Churyukanova, V. Zadorozhnyi, I. Shchetinin and R.K. Roy, *J. Alloys Compd*. 509S, S400 (2011).

[25] M. T. Clavaguera-Mora, N. Clavaguera, D. Crespo and T. Pradell, *Prog. Mater. Sci.* **47**, 559 (2002).

[26] H. A. Shivaee and H. R. M. Hosseini, *Thermochim. Acta* **494**, 80 (2009).

[27] S. Vyazovkin, *J. Comput. Chem.* **18**, 393 (1997).

[28] Y. Yoshizawa, *Mater. Sci. Forum* **307**, 59 (1999).

[29] G. K. Williamson and W. H. Hall, *Acta Metall.* **1**, 22 (1953).

[30] P. Allia, M. Baricco. P. Tiberto and F. Vinai, *J. Appl. Phys.* **74**, 3137 (1993).

[31] K. Song, X. Bian, J. Gu, X. Li, M. Xie and C. Dong, *J. Alloys Compd.* **465**, 7 (2008).

[32] S. Vyazovkin, *Thermochim. Acta* **355**, 155 (2000).

[33] T. Akahira and T. Sunose, *Res. Report Chiba Inst. Technol.* **16**, 22 (1971).

[34] T. Ozawa, *Bull. Chem. Soc. Jpn.* **38**, 1881 (1965).

[35] W. Tang, Y. Liu, H. Zhang and C. Wang, *Thermochim. Acta* **408**, 39 (2003).

[36] A. W. Coats and J. P. Redfern, *Nature* **201**, 68 (1964).

[37] M. J. Starink, *Thermochim. Acta* **404**, 163 (2003).

[38] M. J. Starink, *J. Mater. Sci.* **42**, 483 (2007). [39] S. Vyazovkin and D. Dollimore, *J. Chem. Inf. Comp. Sci.* **36**, 42 (1996).

[40] T. Ungar, G. Tichy, J. Gubicza and R. J. Hellmig, *Powder Diffraction* **20**, 366 (2005).

[41] A. Gupta, M. Jayaraj, S. Lal and R. Verma, *J. Phys. F: Met. Phys.* **18**, 2159 (1988).

[42] D. Jacovkis, J. Rodriguez-Viejo and M. T. Clavaguera-Mora, *J. Phys.: Condens. Matter* **17**, 4897 (2005).

[43] A. R. Yavari and O. Drbohlav, *Mater. Trans. JIM* **36**, 896 (1995).

[44] M. H. Phan, H. X. Peng, M. R. Wisnom, S. C. Yu, N. D. Tho and N. Chau, *Composites Part A* **37**, 191 (2006).

[45] E. Illekova, K. Czomorova, F. A. Kuhnast and J. M. Fiorani, *Mater. Sci. Eng. A* **205**, 166 (1996).

[46] W. Lu, L. Yang, B. Yan and W. Huanga, *J. Alloys Compd.* **420**, 186 (2006).

[47] F. Zhou, K. He and M. Sui, *Mater. Sci. Eng. A* **181-182**, 1419 (1994).

[48] S. Vyazovkin, *Handbook of Thermal Analysis and Calorimetry* (eds. M. E. Brown, P. K. Gallagher), Vol. 5, p. 503, Elsevier B.V. (2008).

[49] V. M. Gorbachev, *J. Therm. Anal.* **8**, 349 (1975).

[50] J. Šesták and G. Berggren, *Thermochimica Acta* **3**, 1 (1971).

[51] M. Baricco, M. Groppi, E. Bosco and A. Castellero, *Mater. Sci. Forum* **360-362**, 445 (2001).

[52] J. D. Ayers, V. G. Harris, J. A. Sprague, W. T. Elam and H. N. Jones, *Acta Mater.* **46**, 1861 (1998).

Table Captions

Table 1. Scattering domain size, crystalline volume fraction and intergranular spacing for F1 and F2 nanocrystalline alloys annealed for 1 hour at the indicated temperatures. The estimated error is about 10%.

Table 2. Magnetic properties measured at 50 Hz of F1 and F2 alloys annealed at 550 °C for 1 hour: Hc, coercivity; Jr, remanence; W, magnetic losses.

Table 1

Temperature (˚C)	Scattering domain size (nm)		Crystalline volume fraction (%)		Intergranular spacing (nm)	
	F1	F2	F1	F2	F1	F2
450	10	18	21	57	5.3	5.2
550	22	26	84	96	2.3	0.7

Table 2

Sample	Hc (A/m)	Jr (T)	W (mJ/kg)
F1	20.6	0.87	9.6
F2	33.9	0.95	18.2

Figure Captions

Fig. 1. X-ray diffraction patterns of the F1, (a), and F2, (b), alloys in the as prepared conditions and after different thermal treatment for 1 hour at the indicated temperatures.

Fig. 2. DSC curves at 20 °C/min of the as prepared F1 and F2 amorphous samples. Onset temperature, peak temperature and heat of the first crystallization peak are indicated.

Fig. 3. TEM bright field images and corresponding SAD patterns of F1 (a) and F2 (b) alloys annealed at 550 °C for 1 hour. The inset of Fig. 3(a) shows the high resolution image of a bcc-(Fe,Si) nanocrystals embedded in the amorphous matrix.

Fig. 4. Hysteresis loop at 50 Hz of F1 and F2 samples after annealing at 550 ˚C for 1 hour.

Fig. 5. DSC curves of the amorphous (a) F1 and (b) F2 amorphous samples at various heating rates.

Fig. 6. Activation energy as a function of transformed fraction for F1 and F2 alloys according to various isoconversional models.

Fig. 7. Variation of the integral form of the reaction model, g(α), as a function of the transformed fraction for F1 (black squares) and F2 (open circles) alloys at 5 °C/min, together with the following theoretical models: power law nucleation controlled reaction (continuous line), three-dimensional phase boundary controlled process (dash-dot-dot light line), one-dimensional diffusion controlled reaction (dot line), two-dimensional diffusion controlled reaction (dash line), three-dimensional diffusion controlled reaction (dash-dot dark line).

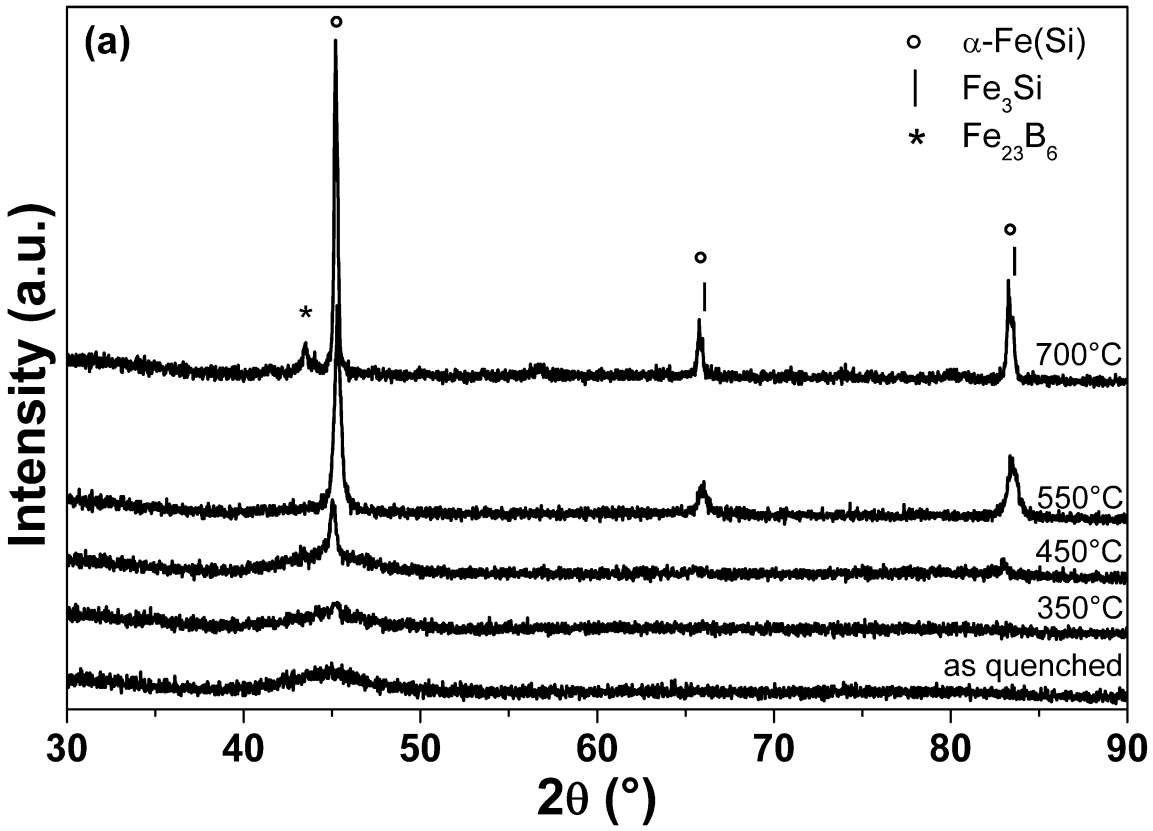
(a)
α-Fe(Si)
Fe3Si
Fe23B6
700°C
550°C
450°C
350°C
as quenched
Intensity (a.u.)
30
40
50
60
70
80
90
2θ (°)

Fig. 1(a)

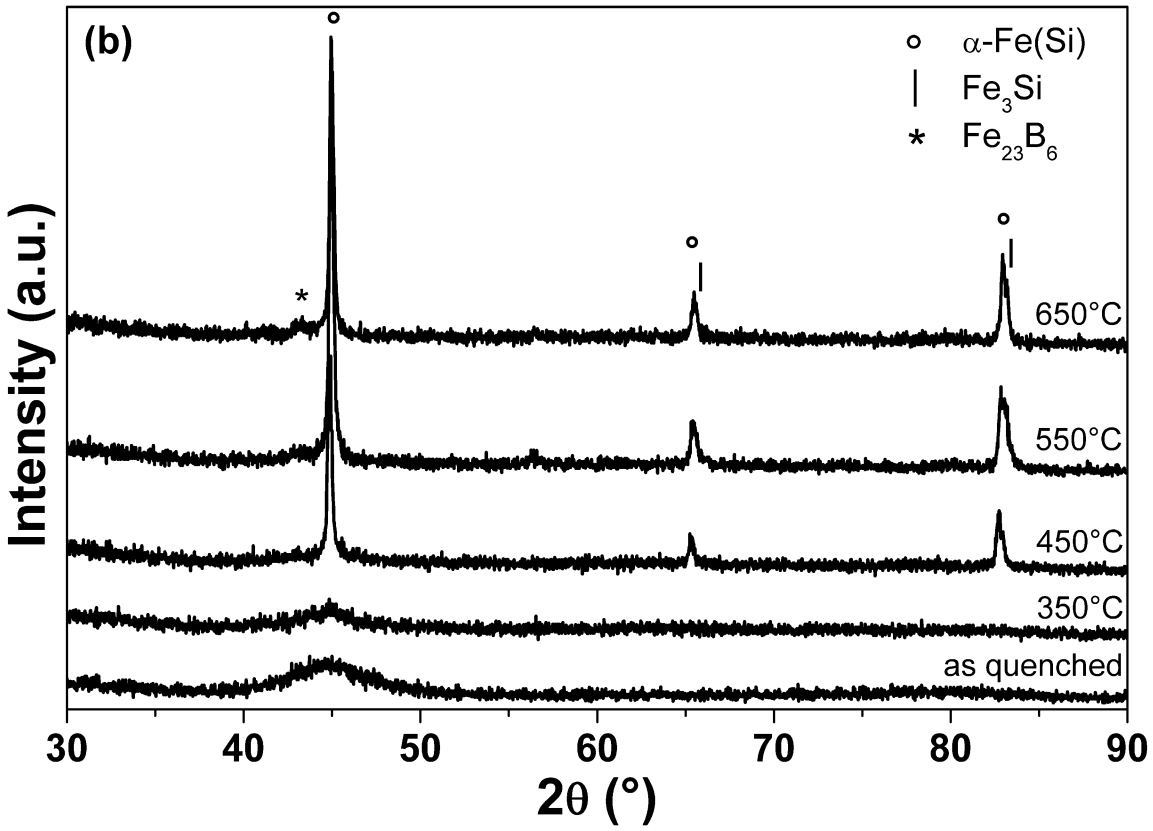
(b)
α-Fe(Si)
Fe3Si
Fe23B6
650°C
550°C
450°C
350°C
as quenched
Intensity (a.u.)
30
40
50
60
70
80
90
2θ (°)

Fig. 1(b)

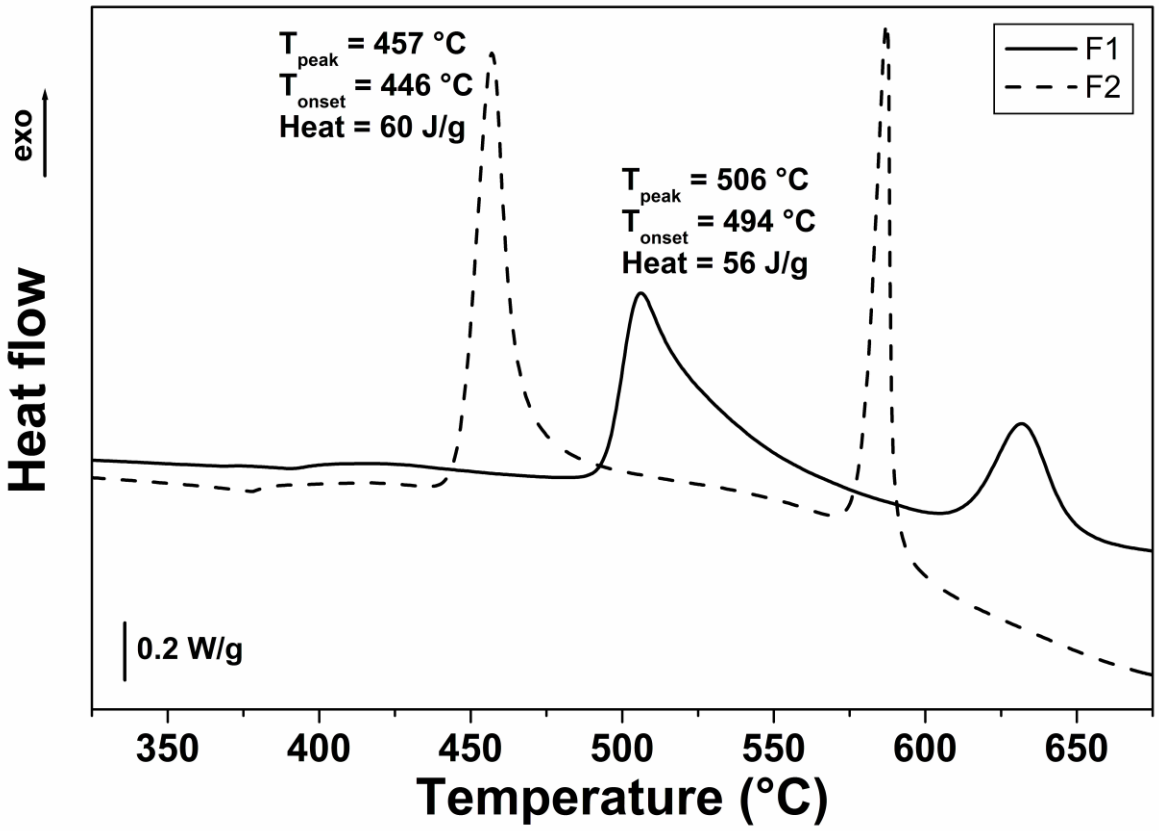
T peak = 457 °C
T onset = 446 °C
Heat = 60 J/g
T peak = 506 °C
T onset = 494 °C
Heat = 56 J/g
F1
F2
exo
Heat flow
0.2 W/g
350
400
450
500
550
600
650
Temperature (°C)

Fig. 2

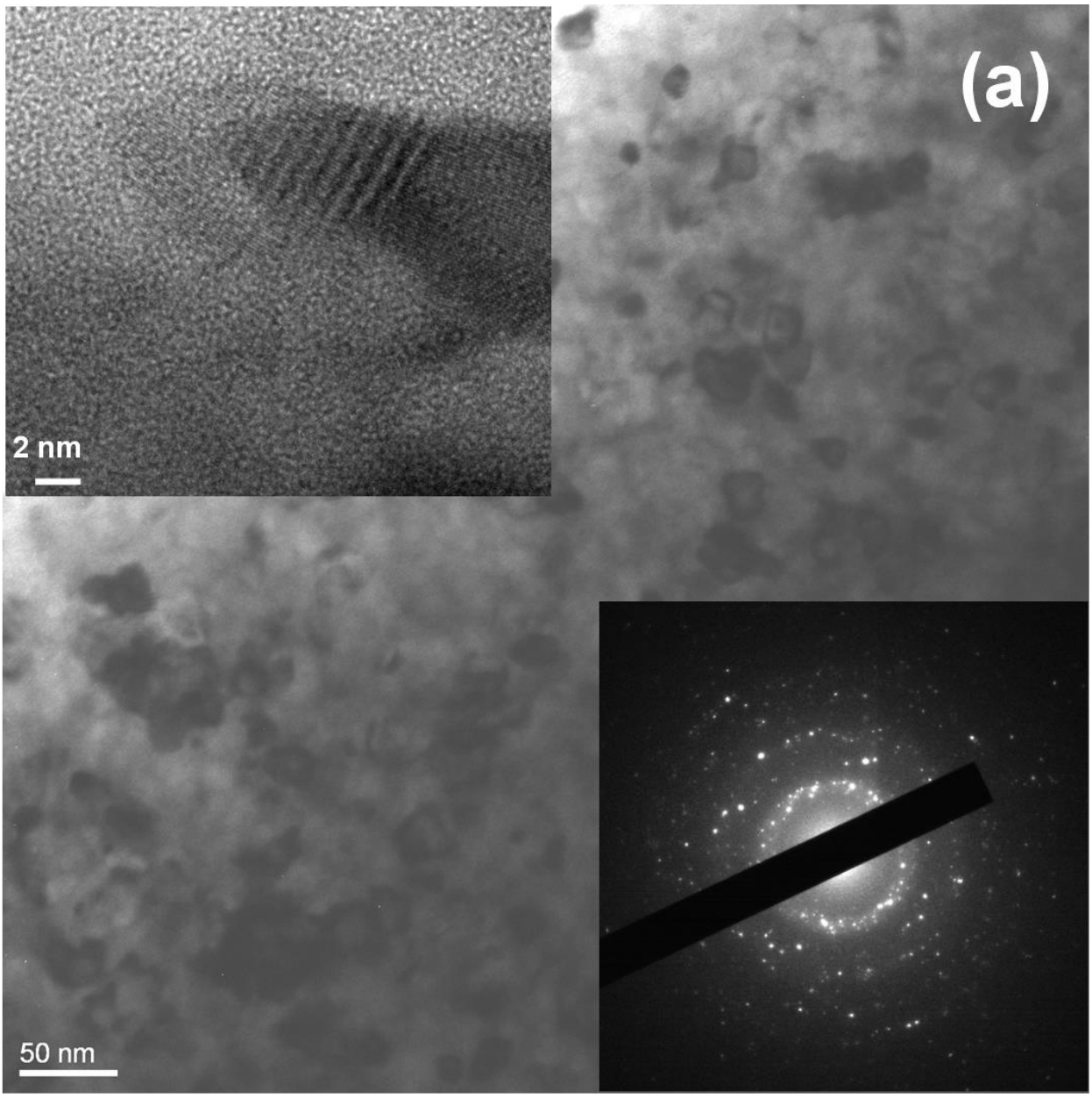

Fig. 3 (a)

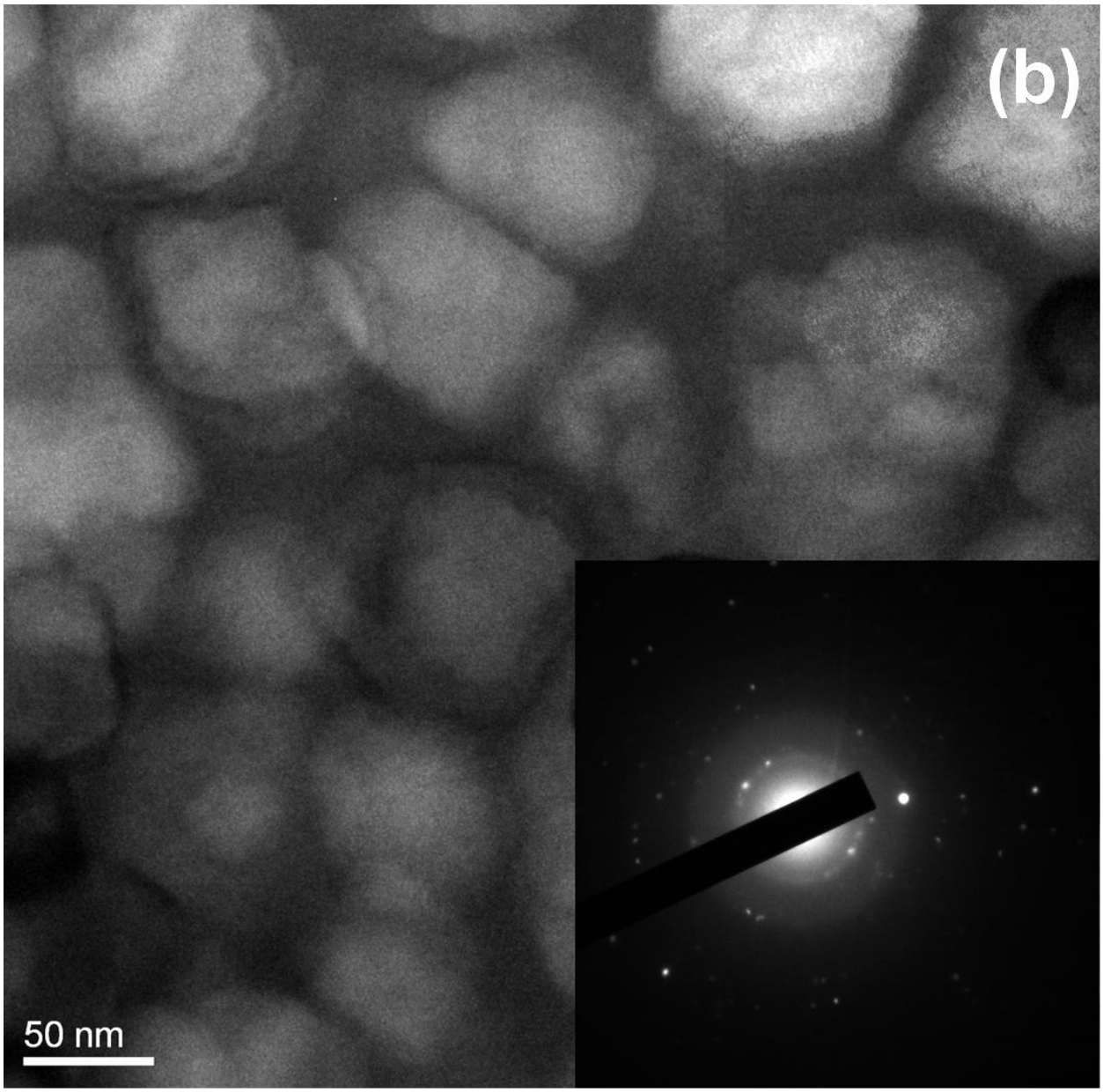

Fig. 3(b)

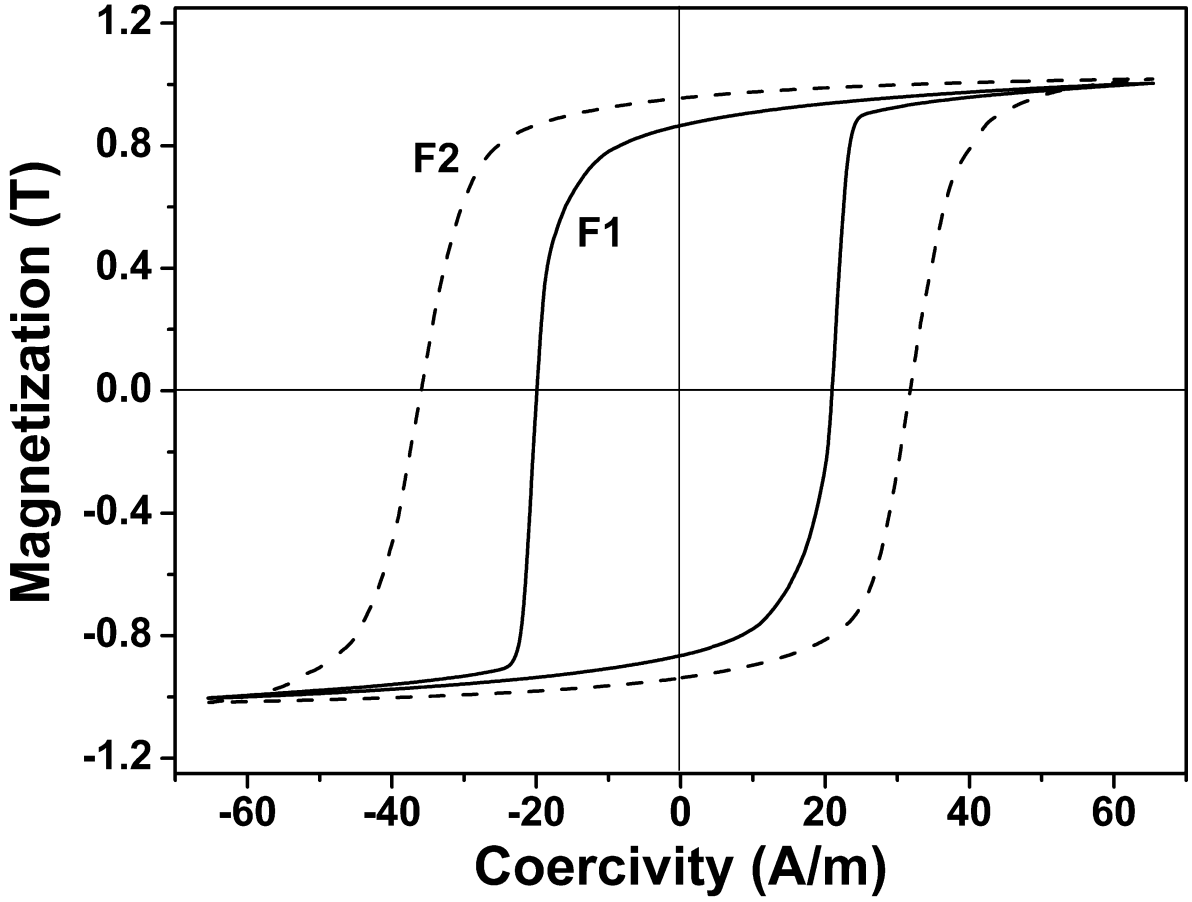
1.2
0.8
0.4
0.0
-0.4
-0.8
-1.2
Magnetization (T)
-60
-40
-20
0
20
40
60
Coercivity (A/m)
F2
F1

Fig. 4

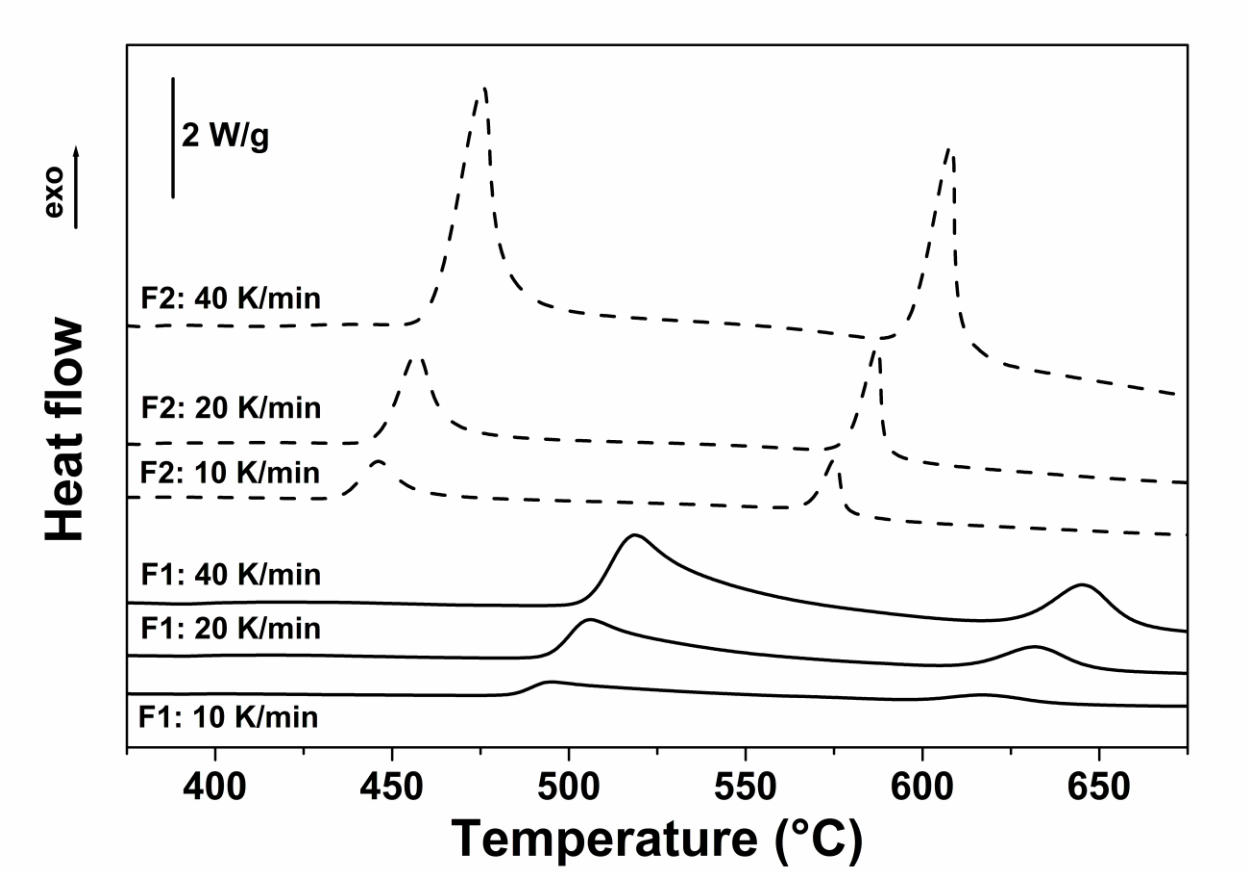
2 W/g
exo
Heat flow
F2: 40 K/min
F2: 20 K/min
F2: 10 K/min
F1: 40 K/min
F1: 20 K/min
F1: 10 K/min
400
450
500
550
600
650
Temperature (°C)

Fig. 5

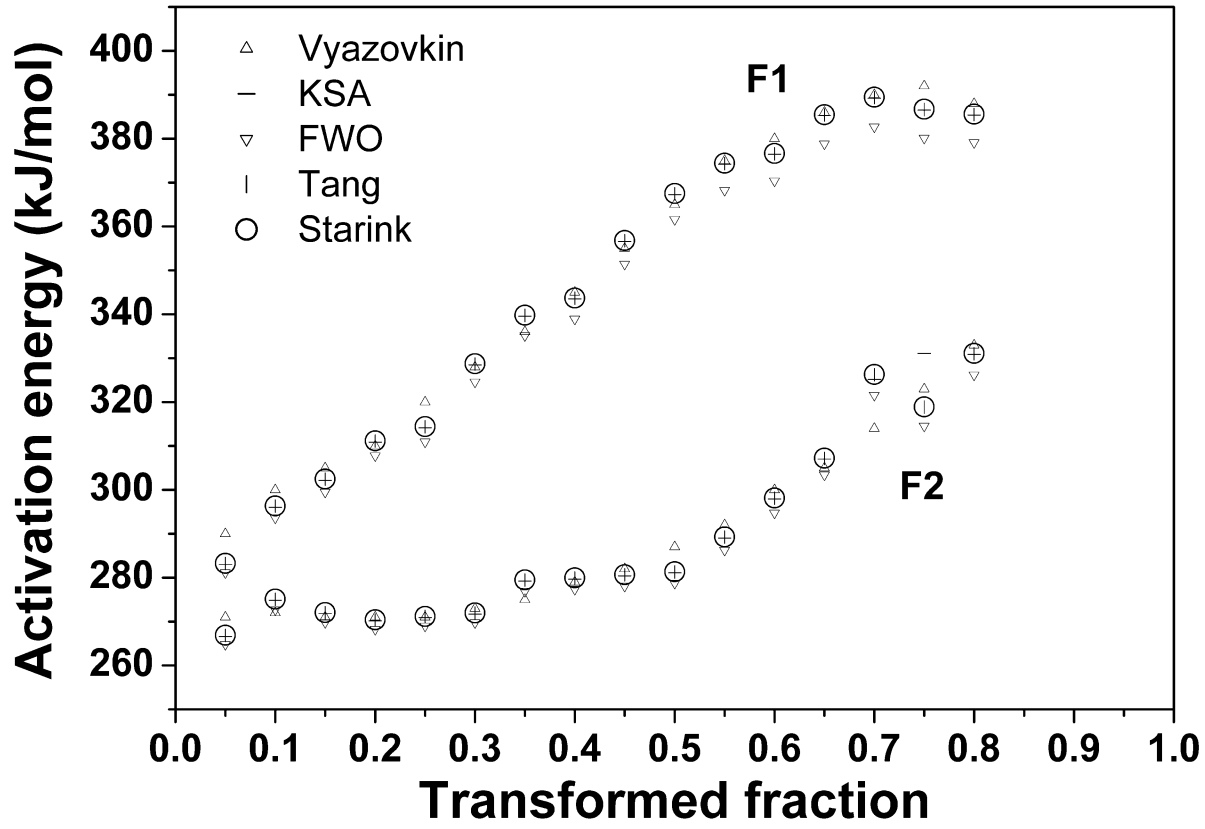
Vyazovkin
KSA
FWO
Tang
Starink
F1
F2
Activation energy (kJ/mol)
Transformed fraction
400
380
360
340
320
300
280
260
0.0
0.1
0.2
0.3
0.4
0.5
0.6
0.7
0.8
0.9
1.0

Fig. 6

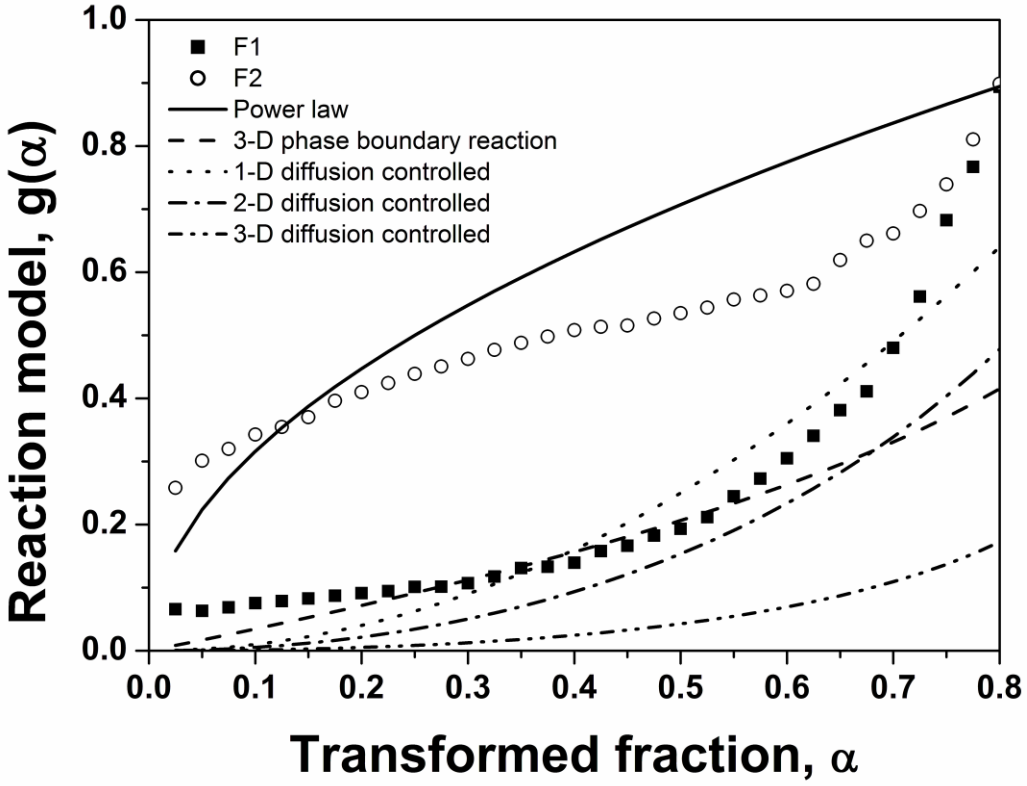
F1
F2
Power law
3-D phase boundary reaction
1-D diffusion controlled
2-D diffusion controlled
3-D diffusion controlled
Reaction model, g(α)
Transformed fraction, α
0.0
0.2
0.4
0.6
0.8
1.0
0.1
0.3
0.5
0.7

Fig. 7